



# High performance misch-metal (MM)-Fe-B magnets prepared by melt spinning



Wen-Liang Zuo <sup>a,b,\*</sup>, Shu-Lan Zuo <sup>a</sup>, Rui Li <sup>a</sup>, Tong-Yun Zhao <sup>a</sup>, Feng-Xia Hu <sup>a</sup>, Ji-Rong Sun <sup>a</sup>, Xue-Feng Zhang <sup>c</sup>, J. Ping Liu <sup>b</sup>, Bao-Gen Shen <sup>a,\*\*</sup>

<sup>a</sup> State Key Laboratory of Magnetism, Institute of Physics, Chinese Academy of Sciences, Beijing, 100190, PR China

<sup>b</sup> Department of Physics, The University of Texas at Arlington, Arlington, TX, 76019, USA

<sup>c</sup> School of Science, Inner Mongolia University of Science and Technology, Baotou, 014010, PR China

## ARTICLE INFO

### Article history:

Received 27 July 2016

Received in revised form

11 October 2016

Accepted 1 November 2016

Available online 3 November 2016

### Keywords:

Misch-metal

High performance

High coercivity

Melt spinning

Permanent magnets

## ABSTRACT

A series of misch-metal (MM = 28.27 wt % La, 50.46 wt % Ce, 5.22 wt % Pr, 15.66 wt % Nd)-iron-boron isotropic ribbons with atomic formula  $(MM)_{12+x}Fe_{82-x-y}B_{6+y}$  ( $x = 0, 1, 2, 3, 4, y = 0, 0.5, 1, 1.5, 2$ ) are prepared by melt spinning technique. A large energy product  $(BH)_{max}$  of 12 MGOe is obtained with the composition of  $MM_{13}Fe_{81}B_6$  at optimized processing. The ribbons with both coercivity larger than 10 kOe and  $(BH)_{max}$  larger than 10 MGOe are achieved in a wide composition range. All the samples exhibit the tetragonal crystal structure. The magnetization and Henkel plot ( $\delta M$ ) measurements indicate that the ribbons have a relatively homogeneous microstructure and strong exchange-coupling interactions. The average grain size of the ribbons is around 30 nm determined via Scherrer's formula. Meanwhile, the transmission electron microscope (TEM) image also verifies that the ribbons have a homogeneous nanoscale microstructure. In addition, the spin reorientation temperature  $T_{sr}$  is investigated by ac susceptibility  $\chi_{ac}$  measurement.

© 2016 Elsevier B.V. All rights reserved.

## 1. Introduction

Permanent magnets are critical for many applications in technology [1,2]. There are two large families on permanent magnet market. One is the ferrite family with low energy product (not over  $38 \text{ kJm}^{-3}$ ) and low price (less than  $\$5 \text{ kg}^{-1}$ ), another is the rare-earth permanent magnets Nd-Fe-B with energy product as high as  $470 \text{ kJm}^{-3}$  and price exceeding  $\$100 \text{ kg}^{-1}$  [1,2]. Therefore, searching for new hard magnetic material with low cost and suitable performance for plugging the gap between the Nd-Fe-B and ferrite magnets becomes important [2]. In fact, "rare-earth" is not really rare in nature, the main problem is the imbalanced use of the elements (the most abundant element Ce is overstock while Nd, Pr and most of the heavy rare-earth elements are understock). On the other hand, environment pollution from extraction process of rare-earths is severe [3,4]. Misch-metal (MM) with the nature ratio

(25–35 wt % La, 45–55 wt % Ce, 4–10 wt % Pr, 14–18 wt % Nd) is a typical representative of the mixed rare-earth elements coexisted in the mines. If Nd can be replaced by MM, the imbalanced use and the environment pollution will be reduced. As a matter of fact, MM-Fe-B material has been studied many years ago, which exhibits excellent intrinsic magnetic properties with larger magnetocrystalline anisotropy field  $H_a$  (40 kOe) and saturated magnetization  $M_s$  (1.26 T) [5–8]. Meanwhile, the magnet of MM based 2:14:1 phase with 8 MGOe energy product has also been prepared [6]. While the sintered magnets exhibit low performance due to the difficulty in obtaining the designed microstructure [9–13]. In addition, because the environment problem has not drawn much attention and the price of rare-earth Nd was not very high before 2011, work on MM-Fe-B materials was suspended. Recently, with the gradually increasing demands of permanent magnets and the pressure from environment protection and the cost of Nd, MM (or Ce)-Fe-B based permanent materials have attracted renewed attention due to the low price and environment-friendly feature [1,3,4,9,13–18]. In this paper, the phase structure, magnetic properties and coercivity mechanism of  $MM_{12+x}Fe_{82-x-y}B_{6+y}$  ( $x = 0, 1, 2, 3, 4, y = 0, 0.5, 1, 1.5, 2$ ) ingots and ribbons have been systematic studied, A large energy product  $(BH)_{max}$  of 12 MGOe is obtained.

\* Corresponding author. State Key Laboratory of Magnetism, Institute of Physics, Chinese Academy of Sciences, Beijing, 100190, PR China.

\*\* Corresponding author.

E-mail addresses: [wzuo@iphy.ac.cn](mailto:wzuo@iphy.ac.cn) (W.-L. Zuo), [shenbg@aphy.iphy.ac.cn](mailto:shenbg@aphy.iphy.ac.cn) (B.-G. Shen).

The ribbons with both coercivity larger than 10 kOe and  $(BH)_{\max}$  larger than 10 MGOe are also achieved in a wide composition range. Meanwhile, the lattice parameters, density and spin reorientation temperature  $T_{sr}$  have also been studied. The MM-Fe-B ribbons with high performance not only can be used as the raw materials of bonded magnets but also can be used for plugging the gap between the Nd-Fe-B and the ferrite magnets.

## 2. Experimentals

$MM_{12+x}Fe_{82-x-y}B_{6+y}$  ( $x = 0, 1, 2, 4, y = 0, 1, 2$ ) compound ingots were prepared by arc-melting in a high purity argon atmosphere. The purity of starting materials is 99% for Fe and 97% for FeB alloys. MM contains about 28.27 wt % La, 50.46 wt % Ce, 5.22 wt % Pr, 15.66 wt % Nd and  $\leq 1$  wt % others. The ingots were melted five times to ensure homogeneity and then annealed at 1173 K for 10 days under vacuum and then rapidly quenched to room temperature. Then a part of the ingots were ground down to less than 150  $\mu\text{m}$  for measure the phase structure and crystal lattice parameters by X-ray powder diffraction (XRD) with Cu K $\alpha$  radiation. Meanwhile, another part of the ingots was used for preparing the ribbons, which were prepared by induction melting the ingot (the weight is about 2 g) in a quartz tube and then ejected onto the surface of a copper wheel with a surface velocity in the range of 20–30 m/s, every sample was prepared with different wheel surface velocity until the preparation condition was optimal (the maximal coercivity is achieved). For  $MM_{12+x}Fe_{82-x}B_6$  ( $x = 0, 1, 2, 4$ ) ribbons, the optimal wheel surface velocity is about 29 m/s, and for  $MM_{12+x}Fe_{82-x-y}B_{6+y}$  ( $x = 1, 2, y = 1, 2$ ) ribbons, the optimal wheel surface velocity is about 30 m/s. The difference of pressure between inside and outside is about 0.6 MPa. The aligned MM-Fe-B resin composite was prepared by mixing the ground MM-Fe-B powders (less than 150  $\mu\text{m}$ ) with epoxy resin and placing them into a 20 kOe magnetic field until the epoxy resin solidifies. Morphology was analyzed by transmission electron microscope (TEM). Magnetic properties were measured by an MPMS with the maximum field of 70 kOe and temperature range of 2–380 K.

## 3. Results and discussion

Fig. 1 shows the measured and refined XRD patterns of heat-treated  $MM_{12+x}Fe_{82-x-y}B_{6+y}$  ( $x = 0, 1, 2, 4, y = 0, 1, 2$ ) ingots at room temperature. All the samples crystallize primarily in the tetragonal crystal structure with space group  $P4_2/mnm$ . For  $y \geq 1$ , the samples show minor impurity of B-rich phase ( $R_{1+x}Fe_4B_4$ ). The refined lattice parameters and density are shown in Table 1. It can be seen that the lattice parameters have a little difference with the changed element composition. With the gradually increased MM, the lattice parameter  $c$  shows a slight decline while  $a$  and  $b$  almost keep constant. However, with the gradually increased element B, the lattice parameters  $a$  and  $b$  show a slight enlargement while  $c$  almost keeps constant. It is known that when the  $R_2Fe_{14}B$  ( $R$  = rare-earth) compounds deviate its stoichiometric composition, especially for more R or B, the R and B will be located in the grain boundary regions to form the grain boundary phase [9,19,20]. After a long time heat treatment, the element of MM (contain La, Ce, Pr, Nd) will take replacement reaction (or interdiffusion) each other, the mechanism is similar to grain boundary diffusion process [19,20], this phenomenon is universal especially for sintered magnets with mixed rare-earth [16,18]. Which leads to the element ratio of main phase grains (or crystal cell) slightly deviation its original ratio, and further results in the slight difference of lattice parameters. This agrees with the results of different  $T_c$  and  $H_a$  of MM-Fe-B magnets with different composition [7]. However, further studies are needed to understand the complex diffusion process.

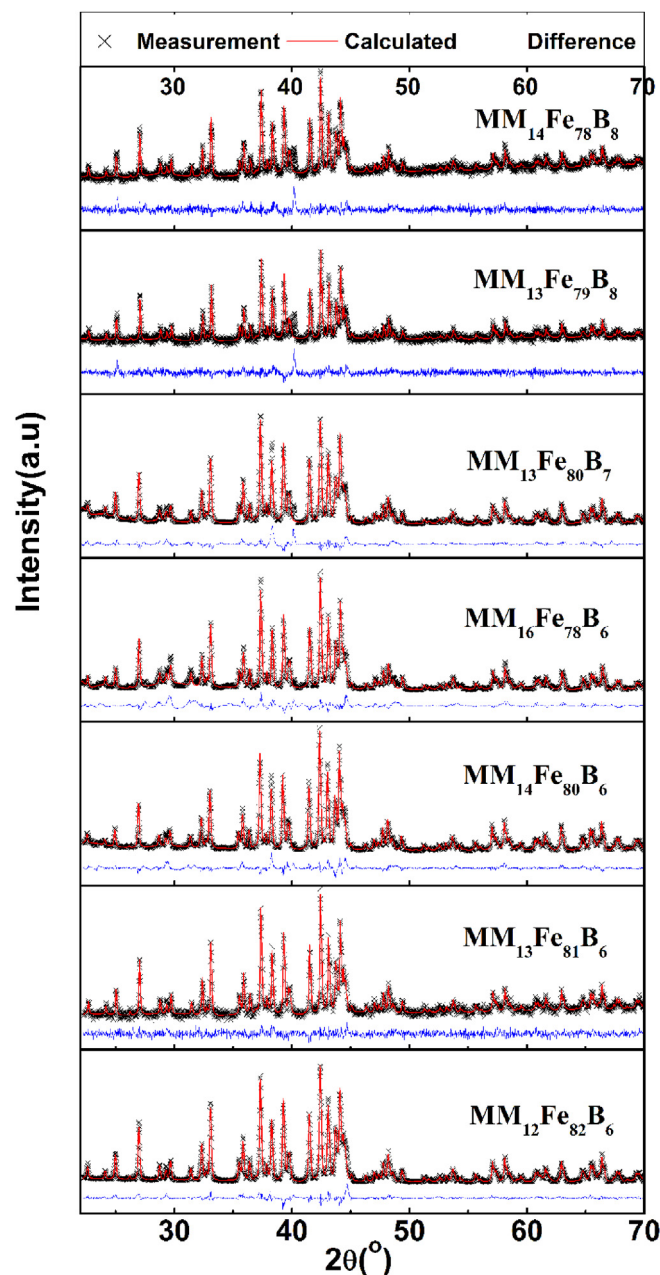


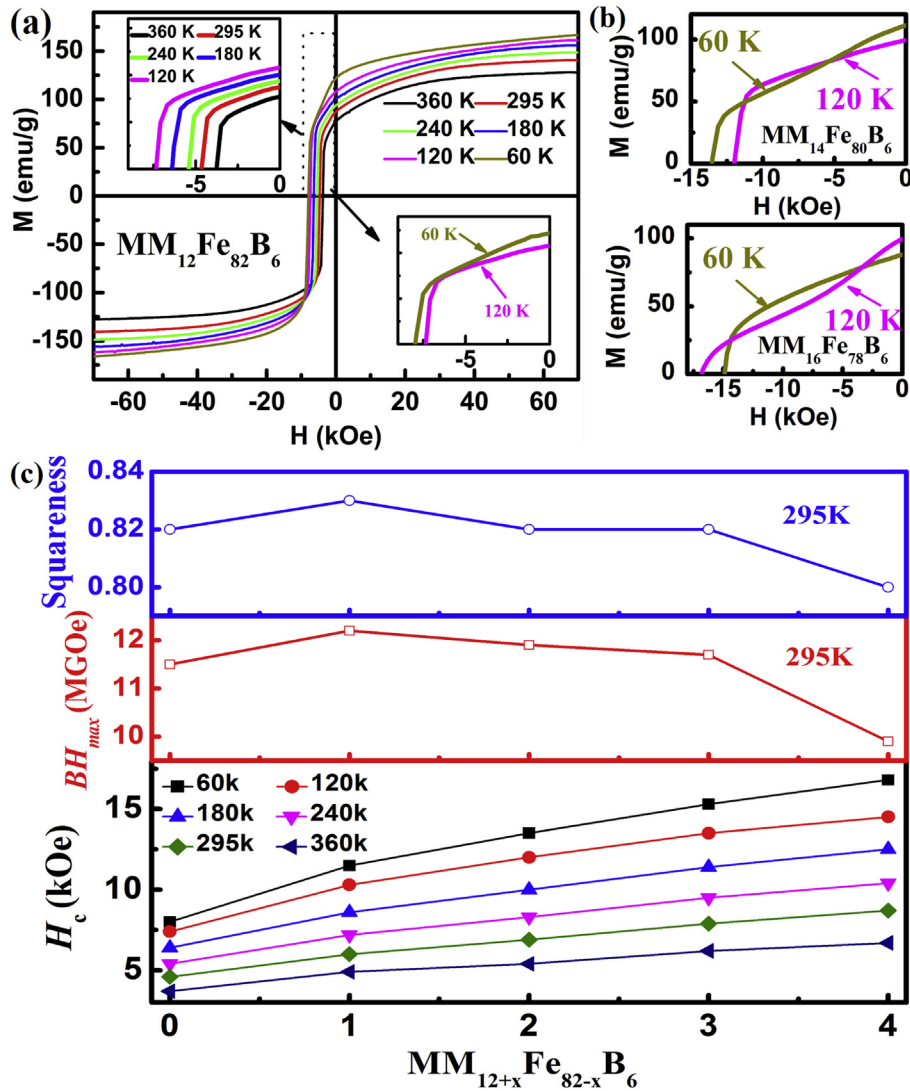
Fig. 1. The measured and refined XRD patterns of heat-treated  $MM_{12+x}Fe_{82-x-y}B_{6+y}$  ( $x = 0, 1, 2, 4, y = 0, 1, 2$ ) ingots.

Table 1

The refined parameters of MM-Fe-B ingots ( $x = 0, 1, 2, 4, y = 0, 1, 2$ ) at room temperature.

samples	$a = b$ (Å)	$c$ (Å)	$R_{wp}$ (%)	$\chi^2$	$\rho$ (g/cm $^3$ )
MM $_{12}$ Fe $_{82}$ B $_6$	8.7763	12.2110	13.0	0.99	7.583
MM $_{13}$ Fe $_{81}$ B $_6$	8.7786	12.2049	14.3	0.94	7.574
MM $_{14}$ Fe $_{80}$ B $_6$	8.7799	12.1847	11.1	1.05	7.589
MM $_{16}$ Fe $_{78}$ B $_6$	8.7796	12.1804	13.6	1.42	7.573
MM $_{13}$ Fe $_{80}$ B $_7$	8.7825	12.1911	11.9	1.79	7.576
MM $_{13}$ Fe $_{79}$ B $_8$	8.7840	12.1912	11.4	1.18	7.574
MM $_{14}$ Fe $_{78}$ B $_8$	8.7823	12.1929	11.6	1.29	7.575

Fig. 2(a) shows the demagnetization curves of  $MM_{12+x}Fe_{82-x}B_6$  ( $x = 0$ ) ribbons measured at different temperature. Samples with  $x = 1, 2, 3, 4$  have a similar variation trend of demagnetization



**Fig. 2.** (a) The demagnetization curves of  $MM_{12}Fe_{82}B_6$  ribbons measured at different temperature, (b) the demagnetization curves of  $MM_{12+x}Fe_{82-x}B_6$  ( $x = 2, 4$ ) ribbons at second quadrant with temperature of 60 and 120 K, (c) the temperature dependence of coercivity; squareness and maximum energy product at 295 K.

curves, thus are not shown here. We only show the difference of demagnetization curves at 60 and 120 K for  $MM_{12+x}Fe_{82-x}B_6$  ( $x = 2, 4$ ) ribbons at the second quadrant (see Fig. 2(b)). The squareness (at 295 K), maximum energy product  $(BH)_{max}$  (at 295 K) and temperature dependence of coercivity are exhibited in Fig. 2(c). The parameters of magnetic properties at 295 K are summarized in Table 2. Firstly, for all the samples, the coercivity shows an almost linear increase with decreasing temperature, due to the gradually increasing magnetocrystalline anisotropy  $H_a$  [7]. In addition, for the samples of  $MM_{12+x}Fe_{82-x}B_6$  ( $x \geq 1$ ), the phenomenon of shoulder is observed in the curves of demagnetization at the low temperature (it is obvious at 60 K, shown in Fig. 2(b)). Furthermore, this phenomenon becomes more and more obvious with the gradually increasing MM due to the gradually reduced exchange-coupling interaction between the MM-Fe-B grains. It is known that the domain wall width is inversely proportional to the  $H_a$  [21]. Therefore, with decreasing temperature (the gradually increasing  $H_a$ ), the domain wall width will decrease, and the effective coupling domain volume will diminish, and the shoulder will be observed and become obvious [21]. Meanwhile, with gradually increasing MM, the grain boundary phase concentration will increase, which

**Table 2**

The grain size and parameters of magnetic property for MM-Fe-B ribbons ( $x = 0, 1, 2, 4, y = 0, 1, 2$ ) at 295 K.

samples	$H_c$ (kOe)	$(BH)_{max}$ (MGOe)	Grain size (nm)	Squareness
$MM_{12}Fe_{82}B_6$	4.6	11.5	$29 \pm 2$	0.82
$MM_{13}Fe_{81}B_6$	6.0	12.2	$31 \pm 1$	0.83
$MM_{14}Fe_{80}B_6$	6.9	11.9	$32 \pm 1$	0.82
$MM_{15}Fe_{79}B_6$	7.9	11.7	$27 \pm 3$	0.82
$MM_{16}Fe_{78}B_6$	8.7	9.9	$33 \pm 1$	0.80
$MM_{13}Fe_{80.5}B_{6.5}$	7.8	11.6	$36 \pm 4$	0.79
$MM_{13}Fe_{80}B_7$	8.5	11.9	$34 \pm 3$	0.75
$MM_{13}Fe_{79.5}B_{7.5}$	9.1	11.8	$35 \pm 3$	0.75
$MM_{13}Fe_{79}B_8$	10.0	11.9	$30 \pm 2$	0.76
$MM_{14}Fe_{79.2}B_{6.8}$	8.5	10.8	–	0.76
$MM_{14}Fe_{79}B_7$	8.7	10.8	–	0.75
$MM_{14}Fe_{78.4}B_{7.6}$	10.1	10.7	–	0.73
$MM_{14}Fe_{78}B_8$	10.1	10.8	–	0.75

reduces the exchange-coupling of MM-Fe-B grains, leading to decoupling evidenced by the shoulder. Here it should emphasize that there is not the phenomenon of shoulder even at the low temperature for the completely homogeneous single phase

materials. Therefore, the appearance of shoulder at low temperature also indicates that the MM-Fe-B ribbons do not have the completely homogeneous nano-size microstructure, this inhomogeneous microstructure could come from both the inhomogeneous grain size and inhomogeneous grain composition (due to interdiffusion), which will be demonstrated in the next section. Moreover, the coercivity shows an almost linear increase with the increasing MM content ( $x \geq 1$ ), which is mainly due to the effect of decoupling due to grain boundary separation [20]. The more interesting phenomenon is that a more obvious increase is observed with increasing MM from 12 to 13. The reason for this increase is complex and could be a multi-factor effect. Firstly, for the sample of  $\text{MM}_{12}\text{Fe}_{82}\text{B}_6$ , it only has very little grain boundary phase in the ribbon, therefore, it is hardly possible for the diffusion to take grain boundary path (relatively low  $H_a$ ). Secondly, because of lack of the grain boundary phase, the effect of decoupling is very weak in this condition. In addition, La and Ce are not easy to form the 2:14:1 phase at the condition of the low rare-earth region [17,22,23], more defects could exist in the  $\text{MM}_{12}\text{Fe}_{82}\text{B}_6$  ribbons. From Table 1 it can be seen that a large energy products  $(BH)_{\text{max}}$  of 12 MGOe is obtained (density  $\rho = 7.58 \text{ g/cm}^3$ ), it is the highest value reported of MM-Fe-B magnets. More importantly, this results imply that the  $(BH)_{\text{max}}$  could exceed 20 MGOe for the anisotropic MM-Fe-B magnet, offering a good possibility for plugging the gap between the Nd-Fe-B and the ferrite magnets. The squareness is obtained by the

ratio of the integral  $\int_0^{-H_c} M dH$  to  $M_r \times H_c$  in the second quadrant of the curve of demagnetization. Which often reflects the uniformity of magnetization reversal, and is also relative to the conditions of exchange-coupling for nanostructured materials. It can be seen that all the samples show the large values of squareness (about 0.8), which indicates that all the samples have a relatively (not completely) homogeneous microstructure and the strong exchange-coupling interaction between the grains. In addition, the squareness increases with increasing  $x$  from 0 to 1 and then decreases when  $x \geq 1$ . The increase is mainly due to the larger  $H_a$  and less defect, and the later decrease is because of the decoupling effect.

In order to further verify the conclusions mentioned above, the XRD of  $\text{MM}_{12+x}\text{Fe}_{82-x}\text{B}_6$  ( $x = 0, 1, 2, 4$ ) ribbons and TEM image of  $\text{MM}_{14}\text{Fe}_{80}\text{B}_6$  ribbon are shown in Fig. 3(a) and (b), respectively. Here we only show the TEM image of  $\text{MM}_{14}\text{Fe}_{80}\text{B}_6$  ribbon, (the TEM image of  $\text{MM}_{15}\text{Fe}_{81}\text{B}_6$  is almost the same as  $\text{MM}_{14}\text{Fe}_{80}\text{B}_6$ ). From Fig. 3(a) it can be seen that all the samples show the tetragonal 2:14:1 phase structure. The average grain size calculated via Scherrer's formula is 29 nm, 31 nm, 32 nm, 27 nm and 33 nm for  $x = 0, 1, 2, 3, 4$ , respectively. The TEM image verifies that the MM-Fe-B ribbons have a relatively homogeneous nanoscale microstructure with average grain size around 30 nm.

As we have declared that all the samples have a relatively homogeneous microstructure and strong exchange-coupling interaction, and it is also known that Henkel plot ( $\delta M$ ) is important and useful in checking the magnetization reversal mechanism and interactions of grains. Therefore, the curves of Henkel plot, which is defined as:  $\delta M = M_d(H) - [1 - 2M_r(H)]$  [24–27], are shown in Fig. 4. Here  $M_r(H)$  is the isothermal remanance (normalizing to  $M_r(H)/M_r(\infty)$ ) acquired after the application and subsequent removal of a field  $H$ ,  $M_d(H)$  is dc demagnetizing remanance (normalizing to  $M_d(H)/M_r(\infty)$ ) acquired after saturation in one direction and then application and removal of a direct field  $H$  in the reverse direction. The positive  $\delta M$  implies that the interactions of grains support the magnetized state and exchange-coupling interaction is dominant, while negative  $\delta M$  means that the interactions promote demagnetized state and the magnetostatic (dipolar) interaction is dominant.

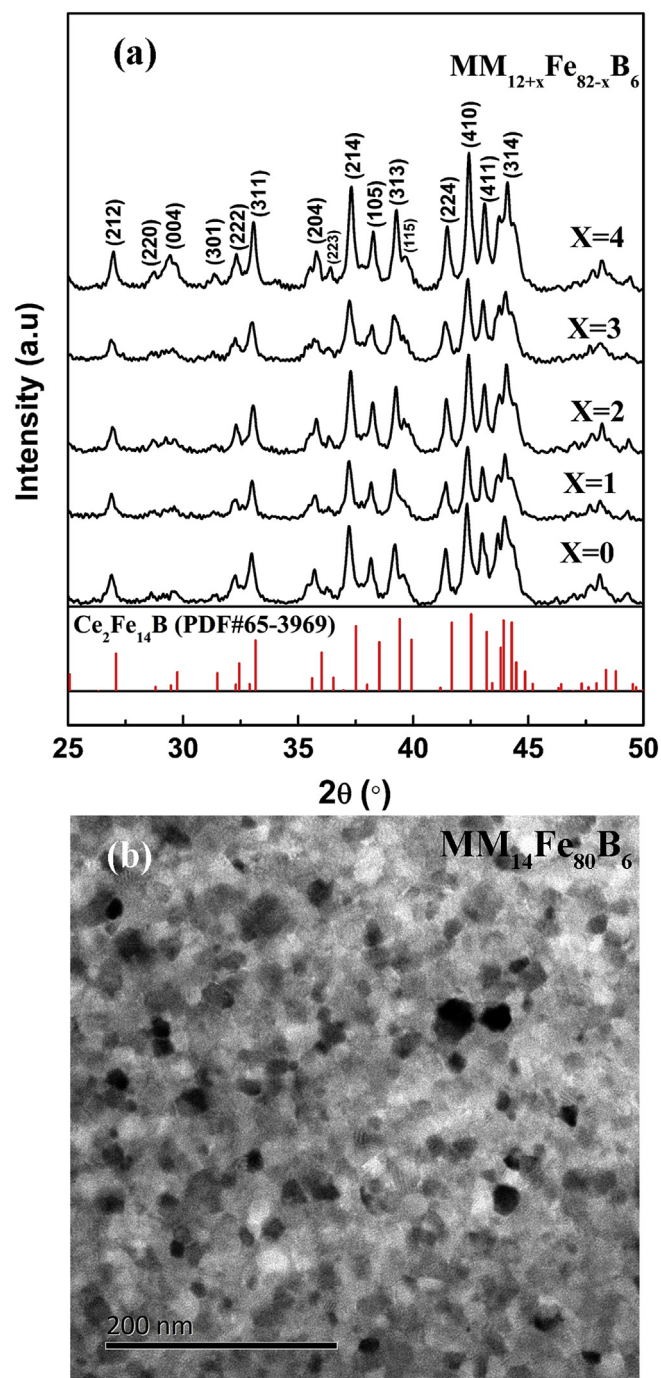


Fig. 3. (a) The XRD patterns of  $\text{MM}_{12+x}\text{Fe}_{82-x}\text{B}_6$  ( $x = 0, 1, 2, 3, 4$ ) ribbons, (b) the TEM image of  $\text{MM}_{14}\text{Fe}_{80}\text{B}_6$  ribbon.

Therefore, the shape of  $\delta M$  often is the results of competition between exchange coupling and magnetostatic (dipolar) interaction. As shown in Fig. 4, all the samples show a positive peak at the field around coercivity, which demonstrates that the exchange-coupling interaction is dominant in the samples. In addition, an increase with increasing MM from 12 to 13 is observed, which agrees with the experiment results of high Ce content ribbons [28,29]. The main reason may be for the fact that the MM facilitates the formation of the 2:14:1 phase, which results in less defects in the  $\text{MM}_{13}\text{Fe}_{81}\text{B}_6$  ribbons [22,23]. And the later decline of  $\delta M$  with  $x \geq 1$  is mainly due

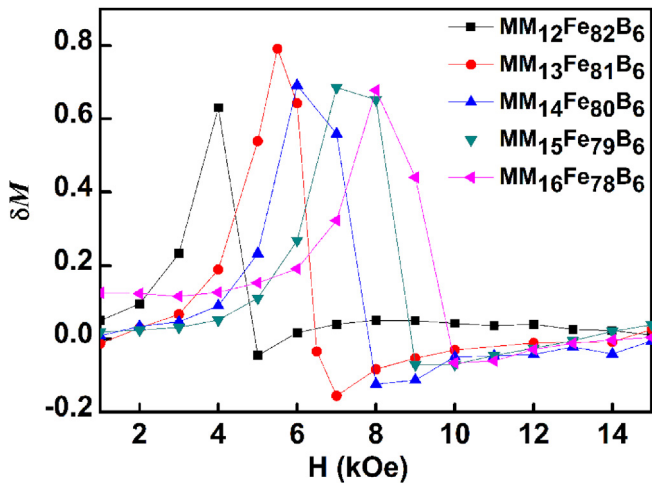


Fig. 4. The Henkel plots ( $\delta M$ ) of  $MM_{12+x}Fe_{82-x}B_6$  ( $x = 0, 1, 2, 3, 4$ ) ribbons.

to the decoupling caused by grain boundary phase, is consistent with the results of the squareness.

The XRD patterns of  $MM_{13}Fe_{81-y}B_{6+y}$  ( $y = 0.5, 1, 1.5, 2$ ) ribbons are shown in Fig. 5. Compared with Fig. 1, it is found that the B-rich phase or impurity peaks ( $R_{1+x}Fe_4B_4$ ) disappeared in the ribbons, which could be due to the fast cooling process that impedes the formation of impurity of B-rich phase ( $R_{1+x}Fe_4B_4$ ) (amorphous), or the content of impurity is too less to be checked by the XRD. The average grain size calculated via Scherrer's formula is 36 nm, 34 nm, 35 nm, 30 nm for  $x = 0.5, 1, 1.5, 2$ , respectively. Which indicates that MM-Fe-B ribbons with B-rich content also have the nanoscale microstructure.

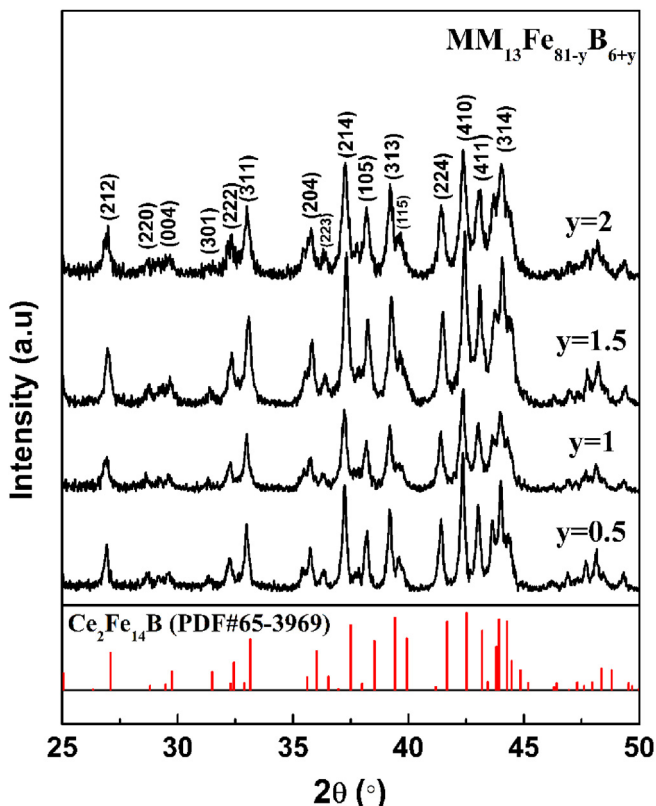


Fig. 5. The XRD patterns of  $MM_{13}Fe_{81-y}B_y$  ( $y = 0.5, 1, 1.5, 2$ ) ribbons.

Fig. 6(a) shows the demagnetization curves of  $MM_{13}Fe_{81-y}B_{6+y}$  ( $y = 0, 1, 2$ ) ribbons at the second quadrant with temperature of 60 and 120 K (the demagnetization curves of other samples have the similar variation trend compared with  $MM_{12}Fe_{82}B_6$  (see Fig. 2(a)), are not shown here). Meanwhile, the squareness (at 295 K), maximum energy product ( $BH$ )<sub>max</sub> (at 295 K) and temperature dependence of coercivity of  $MM_{13}Fe_{81-y}B_{6+y}$  ( $y = 0, 0.5, 1, 1.5, 2$ ) and  $MM_{14}Fe_{80-y}B_{6+y}$  ( $y = 0, 0.8, 1, 1.6, 2$ ) ribbons are shown in Fig. 6(b) and (c), respectively. The parameters of magnetic properties at 295 K are summarized in Table 2. Firstly, as expected, the coercivity shows an increase with increasing Boron content (both for  $x = 1$  and 2), which is mainly due to the effect of decoupling from grain boundary [12], and the coercivity also shows an almost linear increase with decreasing temperature due to the gradually increasing magnetocrystalline anisotropy  $H_a$  [7]. It is interesting to note that the coercivity larger than 10 kOe is observed for the samples of  $MM_{13}Fe_{79}B_8$ ,  $MM_{14}Fe_{78.4}B_{7.6}$  and  $MM_{14}Fe_{78}B_8$ . Furthermore, the

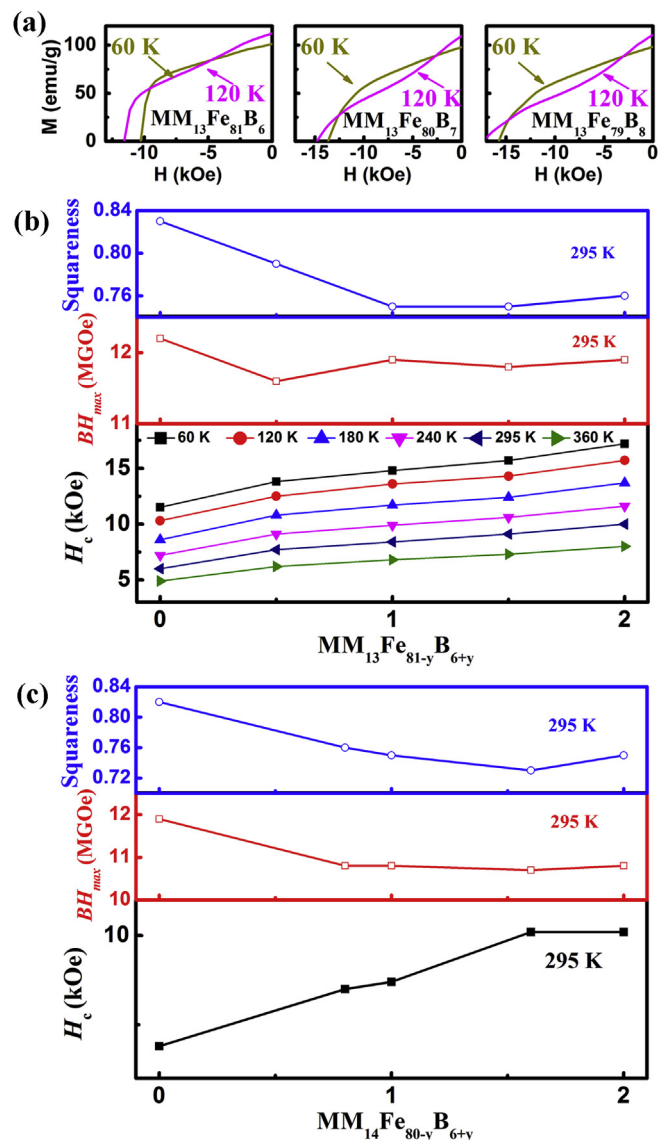


Fig. 6. (a) The demagnetization curves of  $MM_{13}Fe_{81-y}B_{6+y}$  ( $y = 0, 1, 2$ ) ribbons at the second quadrant with temperature of 60 and 120 K. (b) the temperature dependence of coercivity, squareness and maximum energy product at 295 K of  $MM_{13}Fe_{81-y}B_{6+y}$  ( $y = 0, 0.5, 1, 1.5, 2$ ) ribbons, (c) the coercivity, squareness and maximum energy product of  $MM_{14}Fe_{80-y}B_{6+y}$  ( $y = 0, 0.8, 1, 1.6, 2$ ) ribbons at 295 K.

energy products  $(BH)_{\max}$  of all the samples larger than 10 MGOe are obtained for the B-rich  $\text{MM}_{12+x}\text{Fe}_{82-x-y}\text{B}_{6+y}$  ( $x = 1, 2, 1 \leq y \leq 2$ ) ribbons (density  $\rho = 7.58 \text{ g/cm}^3$ ). The excellent permanent magnetic performance appeared in a wide composition range is important for practiced applications, and is a good candidate for plugging the gap between the Nd-Fe-B and the ferrite. Compared with MM-rich MM-Fe-B ribbons, the B-rich ribbons exhibit the relatively poor squareness. The nonuniform reverse magnetization process reveal the relatively weaker exchange-coupling interaction in those samples, leading to the higher coercivity of B-rich MM-Fe-B ribbons. In addition, the more obvious phenomenon of shoulder also verifies the weaker exchange-coupling interaction (see Fig. 6(a)). Here it should be mentioned that the coercivity could not continuously increase for the  $\text{MM}_{12+x}\text{Fe}_{82-x-y}\text{B}_{6+y}$  ( $x = 1, 2$ ) ribbons when  $y \geq 2$  even for  $x \geq 2$ , while the highest coercivity is still about 10 kOe. The detailed magnetic properties of other samples are not shown in the paper.

Fig. 7 shows the temperature dependence on ac susceptibility  $\chi_{\text{ac}}$  of the  $\text{MM}_{13}\text{Fe}_{80}\text{B}_7$  compound. In order to study the spin reorientation temperature  $T_{\text{sr}}$  in detail, the  $\chi_{\text{ac}}$  curves of aligned  $\text{MM}_{13}\text{Fe}_{80}\text{B}_7$  resin composites are also shown. Generally, the  $T_{\text{sr}}$  is reflected by the peak in the  $\chi_{\text{ac}}$  curve [7,30]. It can be seen that a broad peak is observed for the isotropic  $\text{MM}_{13}\text{Fe}_{80}\text{B}_7$  ingot and aligned  $\text{MM}_{13}\text{Fe}_{80}\text{B}_7$  resin composite perpendicular  $c$ -axis direction ( $\perp c$ -axis), while an inflexion is found for the aligned  $\text{MM}_{13}\text{Fe}_{80}\text{B}_7$  resin composite parallel  $c$ -axis direction ( $\parallel c$ -axis). It is known that the position of the peak of  $\chi_{\text{ac}}$  represents the temperature at which the magnetocrystalline anisotropy of the sample is the smallest. It is thus often used for detection the temperature change of easy-magnetization direction (also called spin reorientation). For MM-Fe-B magnets, the element ratio is little different in the grains because of the replacement reaction (or interdiffusion), therefore, the  $T_{\text{sr}}$  should also be different for different grains, which leads to a broad peak appearing in the curve due to the inhomogeneity magnetocrystalline anisotropy of the grains, thus the  $T_{\text{sr}}$  for  $\text{MM}_{13}\text{Fe}_{80}\text{B}_7$  ingot is an average result (about 40 K). For different composition, the average  $T_{\text{sr}}$  should be different, thus  $T_{\text{sr}}$  is around 45, 48, 50 and 51 K for  $\text{MM}_{12}\text{Fe}_{82}\text{B}_6$ ,  $\text{MM}_{14}\text{Fe}_{80}\text{B}_6$ ,  $\text{MM}_{15}\text{Fe}_{79}\text{B}_6$ ,  $\text{MM}_{16}\text{Fe}_{78}\text{B}_6$  compounds, respectively. For the aligned sample, because of the effect of the crystal alignment, the anisotropy field of  $\text{MM}_{13}\text{Fe}_{80}\text{B}_7$  resin composite has been changed compared with the isotropic sample, thus the peak also shows a little difference ( $\perp c$ -axis, about 50 K). In fact, the temperature of practical applications

could be more important for permanent magnetic materials, as it is the on-set temperature from easy magnetization  $c$ -axis (uniaxial anisotropy) to another type of magnetocrystalline anisotropy, which is indicated by the inflexion of  $\chi_{\text{ac}}$  ( $\parallel c$ -axis). And this temperature can also be reflected in the  $\chi_{\text{ac}}$  curves of isotropic and aligned  $\text{MM}_{13}\text{Fe}_{80}\text{B}_7$  resin composite ( $\perp c$ -axis), it is just the end of peaks (around 100 K) which also represents the end temperature from other type of magnetocrystalline anisotropy to uniaxial anisotropy. Therefore, in this paper, the  $T_{\text{sr-end}}$  is defined as the end temperature from other type of magnetocrystalline anisotropy to uniaxial anisotropy (from low temperature to high temperature) or the start temperature from uniaxial anisotropy change to other type of magnetocrystalline anisotropy (from high temperature to low temperature). Although the magnetocrystalline anisotropy fields have a little difference between the grains for the MM-Fe-B materials, the  $T_{\text{sr-end}}$  reflects the highest transition temperature of those grains, thus for MM-Fe-B ( $\text{MM}_{12}\text{Fe}_{82}\text{B}_6$ ,  $\text{MM}_{14}\text{Fe}_{80}\text{B}_6$ ,  $\text{MM}_{15}\text{Fe}_{79}\text{B}_6$ ,  $\text{MM}_{16}\text{Fe}_{78}\text{B}_6$ ,  $\text{MM}_{13}\text{Fe}_{80}\text{B}_7$ ) compounds, all the  $T_{\text{sr-end}}$  are around 100 K.

#### 4. Conclusions

Isotropic MM-Fe-B magnets made from melt spinning with large energy product  $(BH)_{\max}$  up to 12 MGOe have been obtained, which is the highest value reported for the MM-Fe-B magnets. More importantly, the ribbons with both high coercivity (larger than 10 kOe) and high  $(BH)_{\max}$  (larger than 10 MGOe) are also achieved in a wide composition range, which demonstrates that MM-Fe-B is a good candidate for plugging the gap between the Nd-Fe-B and the ferrite. Furthermore, it implies that the  $(BH)_{\max}$  of anisotropy MM-Fe-B magnets could exceed 20 MGOe, which offers promise for developing anisotropic MM-Fe-B based permanent magnets with high performance at low cost. In addition, compared with the traditional Nd-Fe-B, the lower  $T_{\text{sr}}$  is also beneficial for practice applications.

#### Acknowledgement

This work was supported by the National Basic Research Program of China (2014CB643702). National Natural Science Foundation of China (51590880, 51401235 and 51327806). National Key Research Program of China (2016YFB0700903). The Knowledge Innovation Project of the Chinese Academy of Sciences (Grant No. KJZD-EW-M05). Beijing Natural Science Foundation (2152034). China Postdoctoral Science Foundation funded project (2015M581193).

#### References

- [1] A.K. Pathak, M. Khan, K.A. Gschneidner, R.W. McCallum, L. Zhou, K. Sun, K.W. Dennis, C. Zhou, F.E. Pinkerton, M.J. Kramer, *Adv. Mater* 27 (2015) 2663–2667.
- [2] J. Coey, *Scr. Mater* 67 (2012) 524–529.
- [3] M. Zhu, W. Li, J. Wang, L. Zheng, Y. Li, K. Zhang, H. Feng, T. Liu, *IEEE Trans. Magn.* 50 (2014) 1–4.
- [4] X. Wang, M. Zhu, W. Li, L. Zheng, D. Zhao, X. Du, A. Du, *Electron. Mater. Lett.* 11 (2015) 109–112.
- [5] Y.C. Yang, H.Y. Chen, Z.X. Liu, B. Liao, F. Xing, W.W. Ho, *J. Appl. Phys.* 57 (1985) 4115–4117.
- [6] J. Yamasaki, H. Soeda, M. Yanagida, K. Mohri, N. Teshima, O. Kohmoto, T. Yoneyama, N. Yamaguchi, *IEEE Trans. Magn.* 22 (1986) 763–765.
- [7] T. Hien, L. Tai, R. Grössinger, R. Krewenka, F. de Boer, F. Bekker, *J. Less-Common Met.* 127 (1987) 111–116.
- [8] M. Jurczyk, *J. Magn. Magn. Mater* 73 (1988) 199–204.
- [9] E. Niu, Z.-A. Chen, G.-A. Chen, Y.-G. Zhao, J. Zhang, X.-L. Rao, B.-P. Hu, Z.-X. Wang, *J. Appl. Phys.* 115 (2014) 113912.
- [10] W. Gong, G. Hadjipanayis, *J. Appl. Phys.* 63 (1988) 3513–3515.
- [11] K. Ko, S. Yoon, J. Booth, *J. Magn. Magn. Mater* 176 (1997) 313–320.
- [12] K. Ko, S. Yoon, J. Booth, H. Al-Kanani, S. Cho, *J. Mater. Sci.* 37 (2002) 1421–1427.
- [13] K. Ko, S. Yoon, S. Ko, in: *J. Phys. Conf. Ser.*, IOP Publishing, 2011, p. 012036.

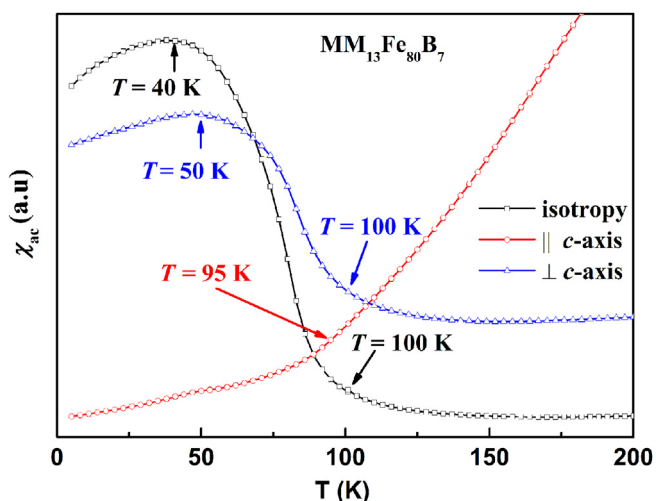


Fig. 7. The temperature dependence on ac susceptibility  $\chi_{\text{ac}}$  of the  $\text{MM}_{13}\text{Fe}_{80}\text{B}_7$  compound.

- [14] A. Alam, M. Khan, R.W. McCallum, D.D. Johnson, *Appl. Phys. Lett.* 102 (2013) 042402.
- [15] E.J. Skoug, M. Meyer, F. Pinkerton, M.M. Tessema, D. Haddad, J. Herbst, *J. Alloys Compd.* 574 (2013) 552–555.
- [16] J. Jin, T. Ma, Y. Zhang, G. Bai, M. Yan, *Sci. Rep.* 6 (2016) 32200.
- [17] A.K. Pathak, K. Gschneidner, M. Khan, R. McCallum, V. Pecharsky, *J. Alloys Compd.* 668 (2016) 80–86.
- [18] E. Isotahdon, E. Huttunen-Saarivirta, V.-T. Kuokkala, *J. Alloys Compd.* 692 (2017) 190–197.
- [19] K. Hirota, H. Nakamura, T. Minowa, M. Honshima, *IEEE Trans. Magn.* 42 (2006) 2909–2911.
- [20] H. Sepehri-Amin, T. Ohkubo, T. Shima, K. Hono, *Acta Mater.* 60 (2012) 819–830.
- [21] J. Liu, Exchange-coupled nanocomposite permanent magnets, in: E. Fullerton, O. Gutfleisch, D.J. Sellmyer (Eds.), *Nanoscale Magnetic Materials and Applications*, Springer, NewYork, 2009, pp. 309–335.
- [22] H. Stadelmaier, N. Liu, N.A. Elmasry, *Mater. Lett.* 3 (1985) 130–132.
- [23] J. Herbst, M. Meyer, F. Pinkerton, *J. Appl. Phys.* 111 (2012) 07A718.
- [24] W.-L. Zuo, M. Zhang, E. Niu, X.-P. Shao, F.-X. Hu, J.-R. Sun, B.-G. Shen, *J. Magn. Mater.* 390 (2015) 15–19.
- [25] T. Thomson, K. O'Grady, *J. Phys. D: Appl. Phys.* 30 (1997) 1566.
- [26] D. Speliotis, W. Lynch, *J. Appl. Phys.* 69 (1991) 4496–4498.
- [27] J. Garcia-Otero, M. Porto, J. Rivas, *J. Appl. Phys.* 87 (2000) 7376–7381.
- [28] M. Zhang, Z. Li, B. Shen, F. Hu, J. Sun, *J. Alloys Compd.* 651 (2015) 144–148.
- [29] Z.-B. Li, M. Zhang, B.-G. Shen, F.-X. Hu, J.-R. Sun, *Mater. Lett.* 172 (2016) 102–104.
- [30] H. Shen, Z. Cheng, F. Hong, J. Xu, X. Wang, J. Wang, Z. Yu, Y. Wang, *J. Alloys Compd.* 680 (2016) 226–231.